Li Guohui (Orcid ID: 0000-0002-9109-7324)
Bai Ling (Orcid ID: 0000-0002-4385-9873)
Ritsema Jeroen (Orcid ID: 0000-0003-4287-7639)

Lateral variations of shear-wave velocity in the D" layer beneath the Indian-Eurasian plate collision zone

Guohui Li[1,2], Ling Bai[1], Jeroen Ritsema[3]

[1]Key Laboratory of Continental Collision and Plateau Uplift, Institute of Tibetan Plateau Research, Center for Excellence in Tibetan Plateau Earth Sciences, Chinese Academy of Sciences, Beijing 100101, China

[2]Institute of Earthquake Forecasting, China Earthquake Administration, Beijing 100036, China

[3]Department of Earth and Environmental Sciences, University of Michigan, Ann Arbor, MI 48109, USA

Corresponding author: Ling Bai (bailing@itpcas.ac.cn)

Key Points

- Using waveforms of S and ScS we estimate the shear-wave velocity (Vs) structure in D" beneath the Indian-Eurasian plate collision zone
- Vs is relatively high overall but we resolve horizontal variations by 3-7% over distances shorter than about 300 km
- Our models place new constraints on geodynamic scenarios for the generation of thermo-chemical heterogeneity in downwelling regions of D''

Abstract

Seismic tomography has demonstrated that the shear-wave velocity is relatively high over a 3,000-km wide region in the lowermost mantle beneath southern and eastern Asia. This seismic anomaly demarcates the current position of slab remnants that may have subducted in the Cretaceous. To further characterize the seismic structure at smaller scales, we measure 929 residual traveltime differences (δt) between the phases ScS and S using recordings of eight earthquakes beneath the Indian Ocean at stations from the Chinese Digital Seismic Network. We interpret variations of δt up to 10 seconds as due to horizontal shear-velocity variations in D" beneath northern India, Nepal, and southwestern China. The shear velocity can vary by as much as 7% over distances shorter than 300 km. Our observations provide additional observational evidence that compositional heterogeneity and possibly melt contribute to the seismic structure of the lower mantle characterized by long-term subduction and mantle downwelling.

Plain Language Summary

Seismic tomography indicates that the seismic wavespeed is relatively high in the lowermost mantle (i.e., the D'' region) beneath regions, such as eastern Asia, influenced by subduction since the Mesozoic era. Our new analysis of the propagation time of shear-wave reflections off the outer core (i.e., the phase ScS) corroborates the result from seismic tomography that the shear velocity in D'' beneath eastern Asia is high overall. However, we also find that the shear velocity can vary by as much as 7% over distances shorter than 300 km within a region of D" beneath northern India, Nepal, and southwestern China. This provides new evidence for the thermo-chemical nature of D'' beneath downwelling regions of the mantle.

1 Introduction

Seismic tomography models agree that the P-wave and S-wave velocities (Vp and Vs, respectively) are relatively high across a wide region of the lowermost mantle beneath eastern and southern Asia (e.g., Houser et al., 2008; Kustowski et al., 2008; Simmons et al., 2010; Ritsema et al., 2011) (Figure 1a). This broad seismic anomaly is the deepest portion of an elongated high-velocity anomaly from southeastern Asia to the Mediterranean at shallower depths in the lower mantle. Reconstruction of paleo-plates linked it to the subduction of the Neo-Tethyan and Pacific plates and the Paleo-Tethyan and Paleo-Pacific plates (e.g., Ricard et al., 1993; Van der Voo et al., 1999; Stampfli & Borel, 2002; Honza & Fujioka, 2004; Muller & Seton, 2015). Thus, the high seismic velocities in D'' beneath eastern and southern Asia are likely related to prolonged subduction in the region and relatively cool fragments of subducted material.

However, seismic tomography and various analyses of teleseismic body waves indicate that Vp and Vs vary also at smaller spatial scales. Studies of teleseismic S wave triplication (e.g., Young & Lay, 1987; Weber & Davis, 1990; Gaherty & Lay, 1992) showed that Vs increases discontinuously by about 2.8% at 280 km above the CMB beneath the Indian Ocean and eastern Eurasia. The waveform complexity suggest that the strength and depth of the discontinuity varies considerably. The discontinuity may be related to the phase transition of perovskite to post-perovskite within a relatively cool lower mantle (e.g., Murakami et al., 2004; Grocholski et al., 2012). Within the wider D'' region of southeastern Asia, there is evidence for anisotropy in Vs (e.g., Ritsema, 2000; Thomas et al., 2007), weak scattering producing PcP precursors (Zhang et al., 2019), albeit not for ultra-low velocity zones at the base of the mantle unless they are thinner than the detection thickness of about 5 km thick (Thorne & Garnero, 2004).

Detailed seismic mapping of D'' beneath Eurasia and other downwelling region is necessary to further evaluate the composition, mineralogy, and structural complexity of the ancient slabs that have accumulated above the core-mantle boundary (CMB). We contribute to such work a study of the arrival-time differences of the phases S and ScS recorded by a network of more than thousand seismic stations in China (Figure 1b). Our unique data enable us to chart 100-km-scale variations of Vs within a 2000×2000 km^2 zone of D'' beneath northern India, Nepal, and southwestern China near the plate boundary of the Neo-Tethys slab.

2 ScS-S differential travel time residuals

2.1 Recorded and synthetic waveforms

The ScS-S difference time is a robust seismic observable and often used to study the seismic structure of the deep mantle. It is less strongly influenced by seismic structure in the upper mantle and by earthquake mislocations than the absolute travel times (e.g., Russell et al., 1998; Wysession et al., 2001; He et al., 2015; Zhao et al., 2017). We measure the arrival times of ScS and S by cross-correlating the

bandpass filtered recorded and computed waveforms to account for all propagation effects on the S and ScS waveforms.

We use ScS and S waveforms recorded by the 1,024 stations from the Chinese Digital Seismic Network (CDSN) (Zheng et al., 2009). The waveform data were produced by eight shallow earthquakes with M_W > 5.6 between 2009 (when the deployment of the CDSN began) and 2018 along the Owen Fracture Zone and beneath the Red Sea (Table S1 and Figure 1b). We determine their focal depths and source mechanisms by modeling the interference of the direct P wave with the pP and sP surface reflections (e.g., Kikuchi & Kanamori, 1986; Bai et al., 2017) (Figure S1) at stations not used in the study of S and ScS. The waveforms have been corrected for the effects of the instrument response.

We calculate synthetic waveforms using the spectral-element method (Komatitsch & Tromp, 2002). The cross-correlation window has a width of 16 s corresponding to the dominant period of the ScS and S waveforms. The cross-correlation function does not change significantly if the time window is up to a factor of two wider (Figure S2). With resources available to us, we can only compute synthetic waveforms with periods longer than 10 s. We apply therefore a second-order Butterworth filter with corner frequencies of 0.02 Hz and 0.1 Hz (i.e., periods of 10−50 s). A filter of 10-50 s results in the sharpest ScS and S pulses and the best imaging results of shear-velocity variations in D'' (Figure S3). We select waveforms in which the S and ScS signals have signal to noise ratios (defined as the square root of the energy ratio of signal to noise) higher than 2.0 and manually checked each waveform to ensure the high quality of data. After these quality checks, we retain 929 transverse-component waveforms for epicentral distances between 46° and 77°.

We retain measurements only if the cross-correlation function has a maximum higher than 0.85 (Figure S4). To quantify the residuals, we consider a 1-D and a 3-D reference model. The reference 1-D profile is AK135 (Kennett et al., 1995). In the reference 3-D model, S40RTS (Ritsema et al., 2011) is the Vs structure in the mantle to a depth of 2591 km and Vs follows the 1-D AK135 profile between 2591 km depth and the CMB. Supplementary Figure S5 compares S40RTS to nine other tomographic models.

2.2 Measurements

We write the traveltime differences between the S wave and the ScS wave in the recorded waveform and synthetic waveform for the reference 1-D profile as ΔS^{1D} and as ΔScS^{1D}, respectively. The residual $\delta t^{1D} = \Delta ScS^{1D} - \Delta S^{1D}$ is the anomaly in the ScS and S arrival time difference with respect to AK135. Similarly, ΔS^{3D}, ΔScS^{3D}, and δt^{3D} denote anomalies in the arrival times of S, ScS and the ScS-S arrival time difference with respect to the 3-D reference model.

Using two examples we illustrate that the measurements of ΔS^{1D}, ΔScS^{1D}, ΔS^{3D}, and ΔScS^{3D} can be significantly different for the two reference models. Figure 2a shows measurements and recorded and synthetic waveforms for Event 4 at station HB.JME at an epicentral distance of 66.7°. The S-wave arrival

3

time is predicted within 1.5 s by either reference model but ScS arrives anomalously early by 3.9 s for the 1-D reference models and 5.5 s for the 3-D reference model. The values for δt^{1D} and δt^{3D} are -2.4 s and -5.9 s, respectively. This demonstrates that the Vs structure of the mantle above D'' has a significant influence on the ScS arrival time in particular. In addition, the 3-D waveform of ScS reproduces the "down-and-up" swing in the recorded ScS waveform better than the 1-D model.

Figure 2b shows the waveforms and modeling results for Event 6 recorded at station HN.CNS at an epicentral distance of 54.0°. The arrival time anomalies of both S and ScS differ by more than 5 s for the 1-D and 3-D reference models. However, δt^{1D} and δt^{3D} are similar at +4.8 and +4.1 s, respectively. This indicates that the ScS-S arrival-time difference is determined primarily by structure in D''.

The values for δt^{3D} for HB.JME (Figure 2a) and HN.CNS (Figure 2b) are extreme values in our collection. The ScS reflection points associated with these two waveforms are [31.7°N, 72.9°E] and [22.3°N, 83.7°E], respectively. If S40RTS is indeed effective in removing the contributions of the mantle above D'' to the ScS-S arrival time difference, the 10-s variation of δt^{3D} for HB.JME and HN.CNS points to a 6% difference in the average Vs velocity in D'' over 800 km.

Figure 3 shows the correlations of ΔS^{1D}, ΔS^{3D}, ΔScS^{1D}, ΔScS^{3D}, δt^{1D} and δt^{3D} for our 929 high-quality measurements. It demonstrates that the anomaly in the ScS-S arrival time difference (i.e., δt^{1D} and δt^{3D}) correlates better with the anomaly in the ScS arrival time (i.e., ΔScS^{1D} and ΔScS^{3D}) (Figure 3b and 3d) than the anomaly in the S arrival time (i.e., ΔS^{1D} and ΔS^{3D}) (Figure 3a and 3c). Further, ΔScS^{3D} correlates better with δt^{3D} than ΔScS^{1D} with δt^{1D} which suggest that using a 3-D reference model is essential in isolating the Vs structure in D'' from the ScS-S arrival time measurements.

3 Modeling

The median value of the 929 measurements of δt^{3D} is -1.75 s (Figure 4a). The predominantly negative values (84% of the total data set) indicates that Vs in the D'' is higher than the AK135 value (and other reference seismic profiles), consistent with the high-velocity anomalies imaged by seismic tomography (e.g., Figure 1a). 95% of all values of δt^{3D} fall between -4.57 s and +1.63 s, indicating that Vs varies significantly in the ScS reflection point region. Part of this signal is an epicentral distance effect; the absolute value of δt^{3D} increases with increasing epicentral distance (Figure S2) because ScS propagates a longer distance through D''.

Since ScS propagates steeply through D'', especially for the shortest epicentral distances, we cannot determine the thickness of D'' and the Vs structure in D'' independently from measurements of δt^{3D}. Therefore, similar to previous studies (e.g., Garnero & Lay, 2003; He & Wen, 2011), we assume that D'' has a uniform thickness, which is 300 km in our case, and adopt a tomographic model, S40RTS in our

4

case, to describe the Vs variation in the mantle above D''. We relate a traveltime anomaly δt^{3D} to a perturbation in Vs in D'' assuming that Vs varies linearly from the AK135 value at 2591 km depth to V_{CMB} at the CMB. We define V_{CMB} by dVs which is the perturbation from the AK135 velocity, V^0_{CMB}, at the CMB. Hence, $V_{CMB} = (1 + dVs) V^0_{CMB}$.

We build a catalog of waveform synthetics for each of the eight earthquakes from Table S1, all stations of the CDSN, and 3-D models in which dVs varies from -5% to +5% with a step of 0.1%. We cross-correlate these waveforms with the waveforms for the 1-D reference model and determine dVs that reproduces δt3D for each of the 929 source-receiver pairs. Because we assume that D'' is 300 km thick, we can only resolve the spatial variations of dVs associated with the variation of δt^{3D}. The range in dVs would be larger or smaller if we had chosen D'' to be thinner or thicker than 300 km, respectively.

Figure 4b shows a map of dVs plotted at the ScS reflection points. Overall, dVs is positive. The highest and lowest values of dVs are +4.2% and -2.8% and resolved in the central portion and near the southeastern margin of the reflection point region separated by less than 300 km. ScS reflection points associated with negative values for dVs are scattered throughout the central portion and form two coherent clusters in the southeastern and westernmost parts of the sampling region, roughly coincident with patches of relative weak Vs perturbations in S40RTS (see Figure 1a).

We show the average values of dVs in Figure 4c. For each average value of dVs, the ScS reflections points fall within a circular cap with a radius of 2°. The cap centers form a 0.5° × 0.5° grid. After averaging, the total variation in dVs is reduced by about a factor of 4 to about -1% to +2% but, as in Figure 4b, dVs appears to be lower within the central portion and lowest in two patches in the southeastern and western parts of the sampling region.

The average values of dVs depend on the assumed cap radius (Figure S6). This indicates that our modeling of δt^{3D} with 1-D profiles of Vs in D'' cannot fully capture the complexity of the data and the sampling of D'' by ScS along non-vertical paths. However, the relatively smooth spatial variation of dVs across the sampling region does not change when the cap radius is larger than 2°. In the smoothest maps, dVs varies by at least 2% over less than 300 km in some parts of the sampling region. These gradients are much stronger than the gradients resolved by S40RTS and other tomographic models.

4 Discussion and Conclusions

Based on the modeling of waveforms of the phases S and ScS produced by earthquakes along the Owen Fracture Zone and beneath the Red Sea and recorded at stations from the Chinese Digital Seismic Network, we constrain ScS-S traveltime (i.e., δt) variations and the 100-km scale Vs structure within a 2000×2000 km^2 zone of D'' beneath northern India, Nepal, and southwestern China near the plate boundary of the Neo-Tethys slab. As expected for a region modified by subduction since the Cretaceous and as imaged consistently by tomographic studies, we find that Vs is high compared to standard seismic

profiles for the lowermost mantle. However, the variation of δt by more than 6 s indicates that horizontal variations of Vs are stronger than can be resolved by seismic tomography.

It is widely recognized that the complex seismic structure implies that D'' is thermo-chemical boundary layer, possibly with distributed partial melts and anisotropy (e.g., Lay et al., 2004). The proposed scenarios by which the heterogeneity is formed are diverse. The seismic heterogeneity may be explained by material left over after Earth's differentiation (e.g., Labrosse et al., 2007; Lee et al., 2010), chemical reactions between the mantle and core (e.g., Dubrovinsky et al., 2003), basalt-harzburgite segregation within the subducted slab that has reached the CMB (e.g., Tackley, 2011; Andrault et al., 2014; Pradhan et al., 2015), enrichment of Fe and Al in post-perovskite (Mao et al., 2014), or with thermal anomalies that may point to incipient plume formation (He et al., 2014).

In the southeastern part of our sampling region, where data coverage is relatively high, horizontal variations in Vs are the strongest. The strength of the horizontal Vs gradients is uncertain because spatial variability in δt is high and the unilateral sampling of D'' for the predominantly southwest-northeast oriented source-receiver combinations necessitates a 1-D modeling of δt. We estimate that Vs changes by 3–7% over distances shorter than 300 km at the CMB, as strong as what has been observed near the margins of large low shear velocity provinces (e.g., Ford et al., 2006; Sun & Miller, 2013). This variation depends on the assumptions of the thickness of D'' and the level at which we average δt. The estimated variation of Vs is higher if they are more strongly concentrated at the CMB. In the extreme case that ultra-low velocity zones are responsible for the variability in δt, their shear velocity reductions must be about 15−35% for thickness between 20−50 km in order to explain a variation of δt of 4 s. We note that there is no evidence for pervasive ULVZs in the lowermost mantle beneath eastern Asia (e.g., Yu & Garnero, 2018). Our work cannot discriminate between geodynamic scenarios for the generation of thermo-chemical heterogeneity in D'' in downwelling regions of the mantle but our seismic modeling indicates that successful models must explain shear-velocity gradients of 3−7% over distances as short as 300 km.

Acknowledgements

References

Andrault, D., Pesce, G., Bouhifd, M. A., Bolfan-Casanova, N., Hénot, J. M., & Mezouar, M. (2014). Melting of subducted basalt at the core-mantle boundary. *Science*, 344(6186), 892-895. http://doi.org/10.1126/science.1250466.

Bai, L., Li, G., Khan, N. G., Zhao, J., & Ding, L. (2017). Focal depths and mechanisms of shallow earthquakes in the Himalayan-Tibetan region. *Gondwana Research*, 41, 390-399. http://doi.org/10.1016/j.gr.2015.07.009.

Chang, S. -J., Ferreira, A. M. G., Ritsema, J., van Heijst, H. J., & Woodhouse, J. H. (2015). Joint inversion for global isotropic and radially anisotropic mantle structure including crustal thickness perturbations. *Journal of Geophysical Research*, 120(6), 4278-4300. https://doi.org/10.1002/2014JB011824.

Dubrovinsky, L., Dubrovinskaia, N., Langenhorst, F., Dobson, D., Rubie, D., Geßmann, C., Abrikosov, I. A., Johansson, B., Baykov, V. I., Vitos, L., Le Bihan, T., Crichton, W. A., Dmitriev, V., & Weber, H.-P. (2003). Iron-silica interaction at extreme conditions and the electrically conducting layer at the base of Earth's mantle. *Nature*, 422, 58-61. https://doi.org/10.1038/nature01422.

Durand, S., Debayle, E., Ricard, Y., Zaroli, C., & Lambotte, S. (2017). Confirmation of a change in the global shear velocity pattern at around 1000 km depth. *Geophysical Journal International*, 211(3), 1628-1639. https://doi.org/10.1093/gji/ggx405.

Ford, S. R., Garnero, E. J., & McNamara, A. K. (2006). A strong lateral shear velocity gradient and anisotropy heterogeneity in the lowermost mantle beneath the southern Pacific. *Journal of Geophysical Research*, 111, B03306. http://dx.doi.org/10.1029/2004JB003574.

Gaherty, J. B., & Lay, T. (1992). Investigation of Laterally Heterogeneous Shear Velocity Structure in D" Beneath Eurasia. *Journal of Geophysical Research*, 97, 417-435. https://doi.org/10.1029/91JB02347.

Garnero, E. J., & Lay, T. (2003). D" shear velocity heterogeneity, anisotropy and discontinuity structure beneath the Caribbean and Central America. *Physics of the Earth and Planetary Interiors*, 140, 219-242. http://doi.org/10.1016/j.pepi.2003.07.014.

Grocholski, B., Catalli, K., Shim, S.-H., & Prakapenka, V. (2012). Mineralogical effects on the detectability of the postperovskite boundary. *Proceedings of the National Academy of Sciences of the United States of America*, 109(7), 2275-2279. http://doi.org/10.1073/pnas.1109204109.

He, Y., & Wen, L. (2011). Seismic velocity structures and detailed features of the D" discontinuity near the core-mantle boundary beneath eastern Eurasia. *Physics of the Earth and Planetary Interiors*, 189(3-4), 176-184. http://doi.org/10.1016/j.pepi.2011.09.002.

He, Y., Wen, L., Capdeville, Y., & Zhao, L. (2015). Seismic evidence for an Iceland thermo-chemical plume in the Earth's lowermost mantle. *Earth and Planetary Science Letters*, 417, 19-27. http://dx.doi.org/10.1016/j.epsl.2015.02.028.

He, Y., Wen, L., & Zheng, T. (2014). Seismic evidence for an 850 km thick low-velocity structure in the Earth's lowermost mantle beneath Kamchatka. Geophysical Research Letters, 41, 7073-7079. http://doi.org/10.1002/2014GL061249.

Honza, E., & Fujioka, K. (2004). Formation of arcs and back-arc basins inferred from the tectonic evolution of Southeast Asia since the Late Cretaceous. *Tectonophysics*, 384(1-4), 23-53. http://doi.org/10.1016/j.tecto.2004.02.006.

Hosseini, K., Matthews, K. J., Sigloch, K., Shephard, G. E., Domeier, M., & Tsekhmistrenko, M. (2018). SubMachine: Web-based tools for exploring seismic tomography and other models of Earth's deep interior. *Geochemistry, Geophysics, Geosystems*, 19, 1464-1483. https://doi.org/10. 1029/2018GC007431.

Houser, C., Masters, G., Shearer, P., & Laske, G. (2008). Shear and compressional velocity models of the mantle from cluster analysis of long-period waveforms. *Geophysical Journal International*, 174(1), 195-212. http://doi.org/10.1111/j.1365-246X.2008.03763.x.

Kennett, B. L. N., Engdahl, E. R., & Buland, R. (1995). Constraints on seismic velocities in the Earth from traveltimes. *Geophysical Journal International*, 122(1), 108-124. http://doi.org/10.1111/j.1365-246X.1995.tb03540.x.

Kikuchi, M., & Kanamori, H. (1986). Inversion of complex body waves-II. *Physics of the Earth and Planetary Interiors*, 43(3), 205-222. https://doi.org/10.1016/0031-9201(86)90048-8.

Koelemeijer, P., Ritsema, J., Deuss, A., & van Heijst, H. J. (2016). SP12RTS: a degree-12 model of shear- and compressional-wave velocity for Earth's mantle. *Geophysical Journal International*, 204, 1024-1039. http://doi.org/10.1093/gji/ggv481.

Komatitsch, D., & Tromp, J. (2002). Spectral-element simulations of global seismic wave propagation-I. Validation. *Geophysical Journal International*, 149(2), 390–412. http://doi.org/10.1046/j.1365-246X.2002.01653.x.

Kustowski, B., Ekstrom, G., & Dziewonski, A. M. (2008). Anisotropic shear-wave velocity structure of the Earth's mantle: A global model. *Journal of Geophysical Research*, 113(B06306). http://dx.doi.org/10.1029/2007JB005169.

Labrosse, S., Hernlund, J. W., & Coltice, N. (2007). A crystallizing dense magma ocean at the base of the Earth's mantle. *Nature*, 450, 866-869. https://doi.org/10.1038/nature06355.

Lay, T., Garnero, E. J., & Williams, Q. (2004). Partial melting in a thermo-chemical boundary layer at the base of the mantle. Physics of the Earth and Planetary Interiors, 146, 441-467. https://doi.org/10.1016/j.pepi.2004.04.004.

Lee, C. T. A., Luffi, P., Höink, T., Li, J., Dasgupta, R., & Hernlund, J. (2010). Upside-down differentiation and generation of a 'primordial' lower mantle. *Nature*, 463, 930-933. https://doi.org/10.1038/nature08824.

Lekić, V., & Romanowicz, B. (2011). Inferring upper-mantle structure by full waveform tomography with the spectral element method. *Geophysical Journal International*, 185(2), 799-831. https://doi.org/10.1111/j.1365-246X.2011.04969.x.

Lu, C., Grand, S. P., Lai, H., & Garnero, E. J. (2019). TX2019slab: A New P and S Tomography Model Incorporating Subducting Slabs. *Journal of Geophysical Research*, 124(11), 11549-11567. https://doi.org/10.1029/2019JB017448.

8

Mao, Z., Lin, J. F., Yang, J., Bian, H., Liu, J., Watsond, H. C., Huang, S., Chen, J., Prakapenka, V. B., Xiao, Y., & Chow, P. (Fe,Al)-bearing post-perovskite in the Earth's lower mantle. *Earth and Planetary Science Letters*, 403, 157-165. https://doi.org/10.1016/j.epsl.2014.06.042.

Moulik, P., & Ekstrom, G. (2014). An anisotropic shear velocity model of the Earth's mantle using normal modes, body waves, surface waves and long-period waveforms. *Geophysical Journal International*, 199, 1713-1738. https://doi.org/10.1093/gji/ggu356.

Muller, R. D., & Seton, M. (2015). Paleophysiography of Ocean Basins. *Encyclopedia of Marine Geosciences*. http://doi.org/10.1007/978-94-007-6644-0_84-1.

Murakami, M., Hirose, K., Kawamura, K., Sata, N., & Ohishi, Y. (2004). Postperovskite phase transition in MgSiO3. *Science*, 304(5672), 855-858. http://doi.org/10.1126/science.1095932.

Panning, M. P., Lekić, V., & Romanowicz, B. A. (2010). Importance of crustal corrections in the development of a new global model of radial anisotropy. *Journal of Geophysical Research*, 115, B12325. https://doi.org/10.1029/2010JB007520.

Pradhan, G. K., Fiquet, G., Siebert, F., Auzende, A., Morard, G., Antonangeli, D., & Garbarino, G. (2015). Melting of MORB at core–mantle boundary. *Earth and Planetary Science Letters*, 431, 247-255. https://doi.org/10.1016/j.epsl.2015.09.034.

Ricard, Y., Richards, M., & Le Stunff, Y. A. (1993). A geodynamical model of mantle density heterogeneity. *Journal of Geophysical Research*, 98, 21,895-21,909. https://doi.org/10.1029/93JB02216.

Ritsema, J. (2000). Evidence for shear velocity anisotropy in the lowermost mantle beneath the Indian Ocean. *Geophysical Research Letters*, 27, 1041-1044. https://doi.org/10.1029/1999GL011037.

Ritsema, J., Deuss, A., van Heijst, H. J., & Woodhouse, J. H. (2011). S40RTS: a degree-40 shear-velocity model for the mantle from new Rayleigh wave dispersion, teleseismic traveltime and normal-mode splitting function measurements. *Geophysical Journal International*, 184, 1223-1236. http://dx.doi.org/10.1111/j.1365-246X.2010.04884.x.

Russell, S. A., Lay, T., & Garnero, E. J. (1998). Seismic evidence for small-scale dynamics in the lowermost mantle at the root of the Hawaiian hotspot. *Nature*, 396, 255-258. http://dx.doi.org/10.1038/24364.

Simmons, N. A., Forte, A., Boschi, L., & Grand, S. (2010). GyPSuM: a joint tomographic model of mantle density and seismic wavespeeds. *Journal of Geophysical Research*, 115(B12310). http://dx.doi.org/10.1029/2010JB007631.

Stampfli, G. M., & Borel, G. D. (2002). A plate tectonic model for the Paleozoic and Mesozoic constrained by dynamic plate boundaries and restored synthetic oceanic isochrones. *Earth and Planetary Science Letters*, 196(1-2), 17-33. https://doi.org/10.1016/S0012-821X(01)00588-X.

Sun, D., & Miller, M. S. (2013). Study of the western edge of the African large low shear velocity province. *Geochemistry Geophysics Geosystems*, 14, 3109-3125. https://doi.org/10.1002/ggge.20185.

Tackley, P. J. (2011). Living dead slabs in 3-D: The dynamics of compositionally-stratified slabs entering a "slab graveyard" above the core-mantle boundary. *Physics of the Earth and Planetary Interiors*, 188, 150-162. https://doi.org/10.1016/j.pepi.2011.04.013.
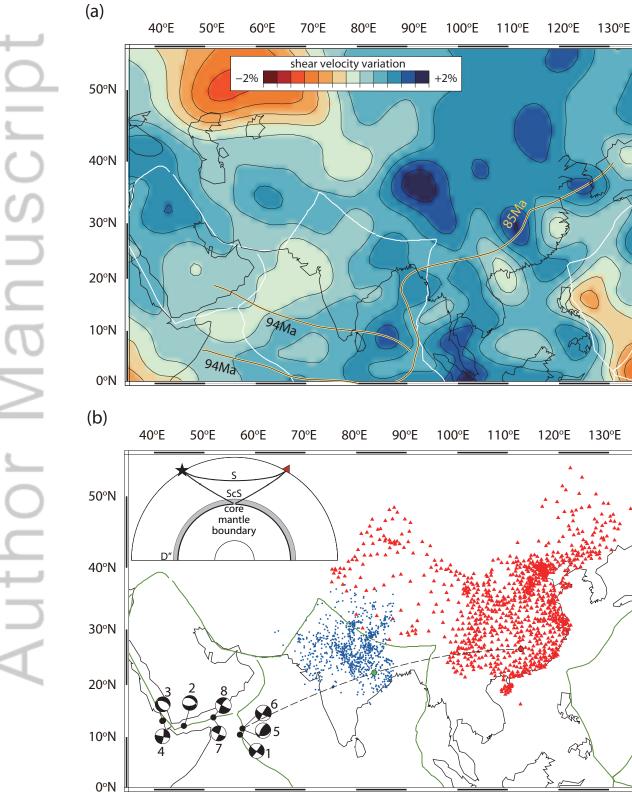
Thomas, C., Wookey, J., & Simpson, M. (2007). D″ anisotropy beneath Southeast Asia. *Geophysical Research Letters,* 34(4), L04301. https://doi.org/10.1029/2006GL028965.

Thorne, M. S., & Garnero, E. J. (2004). Inferences on ultra-low-velocity zone structure from a global analysis of SPdKS waves. *Journal of Geophysical Research*, 109, B08301. https://doi.org/10.1029/2004JB003010.

Van der Voo, R., Spakman, W., & Bijwaard, H. (1999). Tethyan subducted slabs under India. *Earth and Planetary Science Letters*, 171(1), 7-20. https://doi.org/10.1016/S0012-821X(99)00131-4.

Weber, M., & Davis, J. P. (1990). Evidence of a laterally variable lower mantle structure from P- and S-waves. *Geophysical Journal International*, 102, 231-255. https://doi.org/10.1111/j.1365-246X.1990.tb00544.x.

Wessel, P., & Smith, W. H. F. (1998). New, improved version of the generic mapping tools released. Eos. Trans. AGU, 79, 579.

Wysession, M. E., Fischer, K. M., Al-eqabi, G. I., Shore, P. J., & Gurari, I. (2001). Using MOMA broadband array, ScS-S data to image smaller-scale structures at the base of the mantle. *Geophysical Research Letters*, 28(5), 867-870. https://doi.org/10.1029/2000GL008485.

Yong, C. J., & Lay, T. (1987). Evidence for a shear velocity discontinuity in the lower mantle beneath India and the Indian Ocean. *Physics of the Earth Planetary Interiors*, 49, 37-53. http://dx.doi.org/10.1016/0031-9201(87)90131-2.

Yu, S., & Garnero, E. J. (2018). Ultra-low velocity zone locations: A global assessment. *Geochemistry Geophysics Geosystems*, 19, 396-414. https://doi. org/10.1002/2017GC007281.

Zhao, C., Garnero, E. J., Li, M., McNamara, A., & Yu, S. (2017). Intermittent and lateral varying ULVZ structure at the northeastern margin of the Pacific LLSVP. *Journal of Geophysical Research: Solid Earth*, 122, 1198–1220. https://doi.org/10.1002/2016JB013449.

Zhang, B., Ni, S., & Sun, D. (2019). Seismological constraints on the small-scale heterogeneity in the lowermost mantle beneath East Asia and implication for its mineralogical origin. *Geophysical Research Letters*, 46, 5225-5233. https://doi.org/10.1029/2019GL082296.

Zheng, X. F., Ouyang, B., Zhang, D. N., Yao, Z. X., Liang, J. H., & Zheng, J. (2009). Technical system construction of Data Backup Centre for China Seismograph Network and the data support to researches on the Wenchuan earthquake. *Chinese Journal of Geophysics (in Chinese)*, 52(5), 1412-1417. https://doi.org/10.3969/j.issn.0001-5733.2009.05.031.
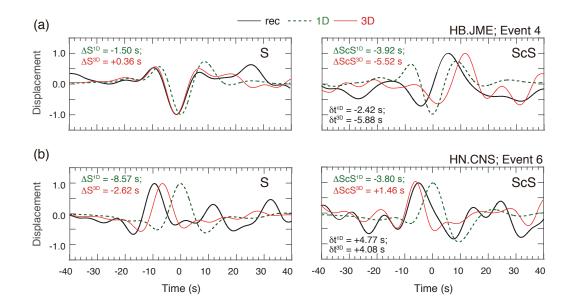
Figure 1. (a) Map of the variation of shear velocity in the lowermost mantle beneath southern Asia according to model S40RTS (Ritsema et al., 2011). The thick line from the eastern Indian Ocean to Korea is the plate boundary between the Pacific and Eurasian plates during the late Cretaceous to the late Eocene (Honza & Fujioka, 2004). Two east-west oriented thick lines beneath the Arabian Sea and the western Indian Ocean are the boundaries of Neo-Tethys Ocean and Eurasian plates during the late Cretaceous (Van der Voo et al., 1999). White lines denote current plate boundaries. (b) Map showing the locations of the eight earthquakes (black circles for the locations; beach balls for the focal mechanisms) and CDSN stations (red triangles) used in this study. The blue circles are the reflection points of 929 ScS phases. Green lines are the present plate boundaries. The dashed line marks the great-circle arc between Event 6 and station HN.CNS. The inset in the upper-left corner shows the S and ScS rays for an epicentral distance of 60°.
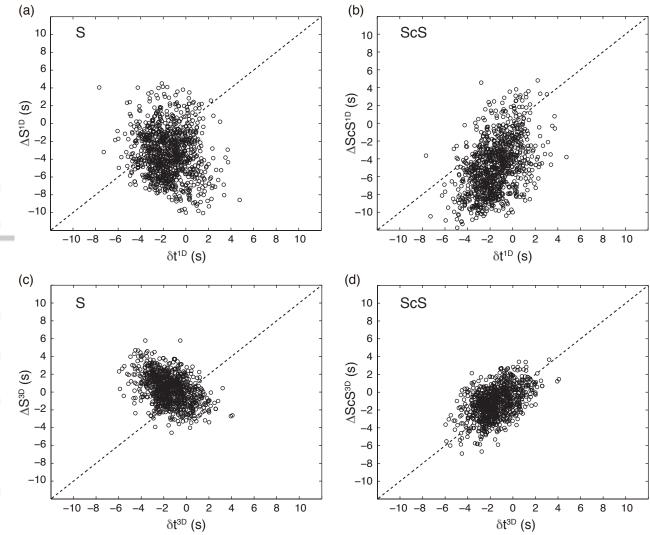
Figure 2. Example of measurements of ΔS^{1D}, ΔScS^{1D}, ΔS^{3D}, and ΔScS^{3D}, indicated in the upper left corners, at stations (a) HB.JME for event 4 and (b) HN.CNS for event 6. The recorded waveform segments are shown with black lines. The synthetics for the 1D and 3D reference models are shown using dashed green and red lines, respectively. The waveforms are 80 s long and have been centered on the AK135 predicted arrival time (at 0 s) of S (on the left) and ScS (on the right). The waveforms have been normalized so their maximum amplitudes are 1.
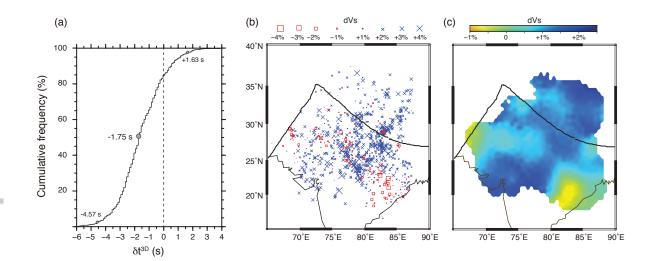
Figure 3. Comparison of the ScS and S arrival time anomalies. (a) ΔS^{1D} versus δt^{1D}, (b) ΔScS^{1D} versus δt^{1D}, (c) ΔS^{3D} versus δt^{3D}, and (d) ΔScS^{3D} versus δt^{3D}.

Figure 4. (a) Cumulative frequency histogram of δt^{3D}. The median value of δt^{3D} is -1.75 s and 95% of the values fall between -4.57 s and +1.63 s. (b) Values of dVs plotted at the CMB reflection points of ScS. Blue crosses and red squares correspond to positive and negative values, respectively. The size of the symbols is proportional to the magnitude of dVs. (c) Map of dVs after cap smoothing using caps with radii of 2° and cap centers spaced every 0.5^o. Each cap contains at least 10 values of dVs.

(a)

(b)

(a)

rec ----- 1D —— 3D

HB.JME; Event 4

$\Delta S^{1D} = -1.50$ s;
$\Delta S^{3D} = +0.36$ s

S

$\Delta ScS^{1D} = -3.92$ s;
$\Delta ScS^{3D} = -5.52$ s

ScS

$\delta t^{1D} = -2.42$ s;
$\delta t^{3D} = -5.88$ s

(b)

HN.CNS; Event 6

$\Delta S^{1D} = -8.57$ s;
$\Delta S^{3D} = -2.62$ s

S

$\Delta ScS^{1D} = -3.80$ s;
$\Delta ScS^{3D} = +1.46$ s

ScS

$\delta t^{1D} = +4.77$ s;
$\delta t^{3D} = +4.08$ s

Time (s)   Time (s)